The Astrophysical Journal, 591:1013–1024, 2003 July 10
© 2003. The American Astronomical Society. All rights reserved. Printed in U.S.A.

[C I] 492 GHz MAPPING OBSERVATIONS OF THE HIGH-LATITUDE TRANSLUCENT CLOUD MCLD 123.5+24.9

F. Bensch,[1,2] U. Leuenhagen,[1,3] J. Stutzki,[1] and R. Schieder[1]

Received 2002 August 2; accepted 2003 March 18

ABSTRACT

We present the first map of the [C I] $^3P_1 \rightarrow {}^3P_0$ fine-structure transition of neutral carbon made toward a translucent molecular cloud (MCLD 123.5+24.9, located in the Polaris Flare). The [C I] observations were made with the *Submillimeter Wave Astronomy Satellite* and are supplemented by ground-based observations of ^{12}CO and ^{13}CO rotational transitions. We find that the [C I] emission is spatially extended following the region bright in ^{12}CO. The [C I] to CO line ratios observed throughout the MCLD 123.5+24.9 cloud are relatively low, and the [C I] line flux density is only ~50% of the emission by the three lowest CO rotational transitions. However, the ratios are still within the range observed along selected lines of sight toward other diffuse and translucent molecular clouds. Assuming LTE conditions for the neutral atomic carbon with an excitation temperature of 8 K derived from the ^{12}CO spectra, we derive a total carbon column density of $(0.25\text{–}1) \times 10^{17}$ cm^{-2} and a C to CO column density ratio between 0.2 and 1.1. Comparison with a photon-dominated region model shows that the model consistently would require uncomfortably high values for the gas volume density in order to reproduce the low [C I] to CO line ratios observed ($n > 10^5$ cm^{-3}), unless we assume that the line-emitting clumps are embedded in an interclump medium with a density of $n < 10^3$ cm^{-3}. The low-density interclump medium does not significantly contribute to the observed [C I] and CO line emission, but the molecular hydrogen in the gas provides an effective shielding for the CO in the embedded clumps by blocking the FUV photons at the frequencies of CO line transition to the predissociation states. This reduces the photodissociation of CO and, thus, the abundance of neutral and ionized carbon in the denser clumps.

Subject headings: astrochemistry — ISM: abundances — ISM: clouds — ISM: individual (MCLD 123.5+24.9) — radio lines: ISM

1. INTRODUCTION

Diffuse and translucent molecular clouds are characterized by low visual extinction of typically a few magnitudes. The gas column density of these clouds is large enough for molecular hydrogen to form but smaller than required to shield CO completely against destruction by photons from the external far-ultraviolet (FUV) field. In contrast to molecular hydrogen and CO where the photodissociation is determined by line absorption, most other molecules are not subject to self-shielding or shielding by more abundant species. Translucent clouds are therefore regions where the heating and the chemistry is governed by the external FUV radiation (van Dishoeck & Black 1986; Hollenbach, Takahashi, & Tielens 1991; Hollenbach, & Tielens 1999).

With some of the translucent and diffuse clouds possibly representing early stages of molecular cloud formation, an even higher fraction of carbon is expected to be in neutral form. Time-dependent models (Störzer, Stutzki, & Sternberg 1997) show that for molecular clouds that are suddenly shielded from the incident FUV flux, the initially abundant C^+ ions rapidly recombine, while the neutral carbon is much more slowly incorporated into CO. In this phase, the [C I] fine-structure emission is significantly brighter than predicted by chemical equilibrium models. [C I] observations are therefore useful for detecting young molecular material where the commonly used molecular cloud tracers such as the CO rotational transitions are weak or undetectable.

Translucent regions are also found close to the surface of molecular clouds with larger visual extinction and with most of their carbon in CO. Embedded in the mean interstellar radiation field, the chemistry in a layer with $A_V \lesssim 3$ is dominated by the external FUV field, similar to translucent clouds. This layer marks the transition region of carbon, which is singly ionized at its surface and bound in CO at $A_V \gtrsim 3$. While H_2 is the most abundant species in this transition layer, photoreactions maintain a relatively high abundance of ionized and neutral carbon, giving a detectable signal for the [C II] and [C I] fine-structure transitions. Translucent clouds and cloud surfaces might therefore be considered as photon-dominated regions (PDRs) generated by a weak ambient FUV field of the order of the mean interstellar radiation field (ISRF). Toward larger optical depths, most of the carbon is converted to CO, and the abundance of neutral and ionized carbon is expected to drop by several orders of magnitude. However, it is not entirely clear if non-equilibrium processes such as bistability (Le Bourlot et al. 1993) and dynamical mixing (Chièze, Pineau des Forêts, & Herbst 1991) can maintain a larger abundance of neutral carbon even in shielded regions.

With neutral carbon being abundant in translucent clouds and cloud surfaces, the [C I] transitions can be used as diagnostic tool for the processes governing the interaction between molecular clouds and the ambient medium. Observations of [C I] help to address questions related to the formation of molecular clouds, their composition, and structure. Gas cooling in PDRs is dominated by the fine-structure lines of neutral oxygen and ionized carbon and

[1] Physikalisches Institut der Universität zu Köln, Zülpicher Strasse 77, 50937 Cologne, Germany.
[2] Harvard-Smithsonian Center for Astrophysics, 60 Garden Street, Cambridge, MA 02138.
[3] L. B. Kiel, Martensdamm 6, 24103 Kiel, Germany.

CO rotational transitions. Cooling by the [C I] fine-structure transitions, however, can become important for clouds in the ISRF and even dominate for cloud densities of the order of few 10^3 cm^{-3} (Kaufman et al. 1999).

The first detection of [C I] emission at 492 GHz for a diffuse molecular cloud was made by Keene, Blake, & Phillips (1987) with the Kuiper Airborne Observatory toward the line of sight of ζ Oph. More detailed studies of the faint [C I] emission from translucent clouds became feasible with the advent of sensitive submillimeter receivers for ground-based observatories (e.g., the Caltech Submillimeter Observatory, the James Clerk Maxwell Telescope, Antarctic Submillimeter Telescope and Remote Observatory and Heinrich Hertz Submillimeter Telescope). These studies derive a C to CO abundance ratio between 0.1 and 2 for translucent clouds and cloud edges (Ingalls, Bania, & Jackson 1994; Stark et al. 1996; Ingalls et al. 1997) and larger ratios for diffuse clouds (Stark & van Dishoeck 1994). The cooling by [C I] is found to be of the same order or even larger than the cooling by low-J CO rotational transitions (Heithausen et al. 2001).

The [C I] studies made for diffuse and translucent clouds are, however, limited to a few positions for each source, mainly observed toward the core of the cloud. Only little is known on the larger scale distribution of their [C I] emission, and it is not clear if the results derived for the individual positions are representative for the whole cloud. The large-scale [C I] emission has been studied for a number of dark clouds and giant molecular clouds (Plume, Jaffe, & Keene 1994; Maezawa et al. 1999; Tatematsu et al. 1999; Plume et al. 2000). The mapping of extended areas for translucent clouds, however, is much more difficult because their [C I] emission is much fainter than for the former class of objects. It requires stable atmospheric conditions over a long period, making it very difficult for ground-based observatories.

Here we report the observation of the [C I] $^3P_1 \rightarrow {}^3P_0$ transition made with the *Submillimeter Wave Astronomy Satellite* (*SWAS*) toward the translucent cloud MCLD 123.5+24.9. The absence of atmospheric extinction, the relatively large main beam width ($\sim$4.′3), and high beam efficiency (0.9) makes *SWAS* an ideal instrument to map weak [C I] emission. In § 2, we summarize the properties of MCLD 123.5+24.9 and present the [C I] and CO observations. In § 3, we use the LTE approximation to derive column densities, the C to CO ratio, and determine the contribution of the [C I] transitions to the gas cooling. In § 4, we compare the observations to results from a spherical PDR model, followed by a discussion of the results in § 5. A summary is given in § 6.

2. OBSERVATIONS

2.1. *MCLD 123.5+24.9*

The high-latitude cloud MCLD 123.5+24.9 is a prominent local maximum in the ^{12}CO $J = 1 \rightarrow 0$ integrated intensity map of the Polaris Flare (Heithausen & Thaddeus 1990). Zagury, Boulanger, & Banchet (1999) used the $E(B–R)$ color excess observed toward background stars to derive a visual extinction map with an angular resolution of 5′. The A_V varies between $\sim$0.5 for the region with the weakest CO emission in Figure 1 to $A_V \sim 2$ toward the cloud center and classifies MCLD 123.5+24.9 as a translucent molecular cloud. The mean neutral hydrogen column density observed toward the cloud is $N_{\rm H} \approx 8 \times 10^{20}$ cm^{-2} (Meyerdierks, Heithausen, & Reif 1991), corresponding to $A_V \approx 0.5$.

Distance estimates for the cloud range between 100 and 250 pc (Heithausen & Thaddeus 1990; Zagury, Boulanger, & Banchet 1999). We adopt $d = 150$ pc for the following and rescaled all distance-dependent quantities taken from the literature accordingly. This places the cloud well into the Galactic molecular disk, despite its high Galactic latitude of $b = 24.^\circ9$. The FUV field at the location of the cloud is expected to be on the order of the ISRF, $\chi \sim \chi_0$, where $\chi_0 = 2.0 \times 10^{-4}$ ergs s^{-1} cm^{-2} sr^{-1} (Draine 1978). This is supported by the results of Zagury, Boulanger, & Banchet (1999) and Bernard et al. (1999), who find that the ambient radiation field at the cloud is not significantly elevated or reduced compared to the ISRF.

Grossmann et al. (1990) mapped the $J = 1 \rightarrow 0$ transition of ^{12}CO and ^{13}CO and derive a total cloud mass of $M \approx 18\ M_\odot$ for MCLD 123.5+24.9, more than 10 times smaller than its virial mass. The mean density of the cloud is $n \approx 500$ cm^{-3}. Observations of ^{13}CO and C^{18}O made with an angular resolution below 1′ reveal several cores with a factor of 10–100 higher volume densities (Grossmann et al. 1990) and significant substructure down to linear scales possibly as small as 200 AU (Falgarone et al 1998). The CO excitation condition derived for the core at ($\Delta l = 0.'0$, $\Delta b = -1.'8$) in Figure 1 is characterized by $n \approx 10^4$ cm^{-3} and $T_{\rm ex} = 8$–9 K ($M_{\rm core} \approx 1.3\ M_\odot$). Observations of CS and HC_3N rotational transitions and dust continuum at millimeter wavelengths indicate the presence of gas with very high densities, $n \sim 10^5$ cm^{-3} (Heithausen, Bertoldi, & Bensch 2002). However, the core and the region outlined by the high-density tracers have an angular extent of $4.'2 \times 0.'7$ (0.18×0.03 pc). At larger spatial scales, and thus at the angular scale of the *SWAS* observations, a density closer to the cloud volume average of $n \sim 500$ cm^{-3} should be applicable.

Spectral line studies made for the dense core in a large number of species reveal a complex chemistry with a high abundance of CS and SO (Grossmann & Heithausen 1992; Gerin et al. 1997), and Heithausen, Corneliussen, & Grossmann (1995) conclude that sulfur must be essentially undepleted in the gas phase. This is essential for the PDR model discussed in § 4 below, as sulfur is important to the formation of neutral carbon in the surface layer of molecular clouds (Tielens & Hollenbach 1985; Sternberg & Dalgarno 1995).

2.2. *Neutral Carbon and* CO *Observations*

The *SWAS* [C I] $^3P_1 \rightarrow {}^3P_0$ observations toward MCLD 123.5+24.9 were made between 1999 September and 2000 April. (See Melnick et al. 2000 for a description of the *SWAS* instrument and the details of the data acquisition and reduction.) They were made in nodding mode, switching between the on position and a signal-free reference. The on positions cover a rectilinear grid centered on R.A. = $02^{\rm h}00^{\rm m}0.^{\rm s}7$ and decl. = 87°42′04″ (J2000; Galactic coordinates: $l = 123.^\circ68$, $b = 24.^\circ93$), with the major axis being defined by the local directions of R.A. and decl. at this position. (Note the significant curvature of the [projected] equatorial coordinates toward the Polaris Flare, close to the north Celestial pole.) The spacing of the observations is 3.′2, slightly smaller than the FWHM of the elliptical *SWAS* beam ($3.'8 \times 5.'0$; main beam efficiency, $B_{\rm eff}/F_{\rm eff} = 0.9$). The on-source integration time of the spectra is between 20 and 200 minutes (average 79 minutes), with deeper integrated

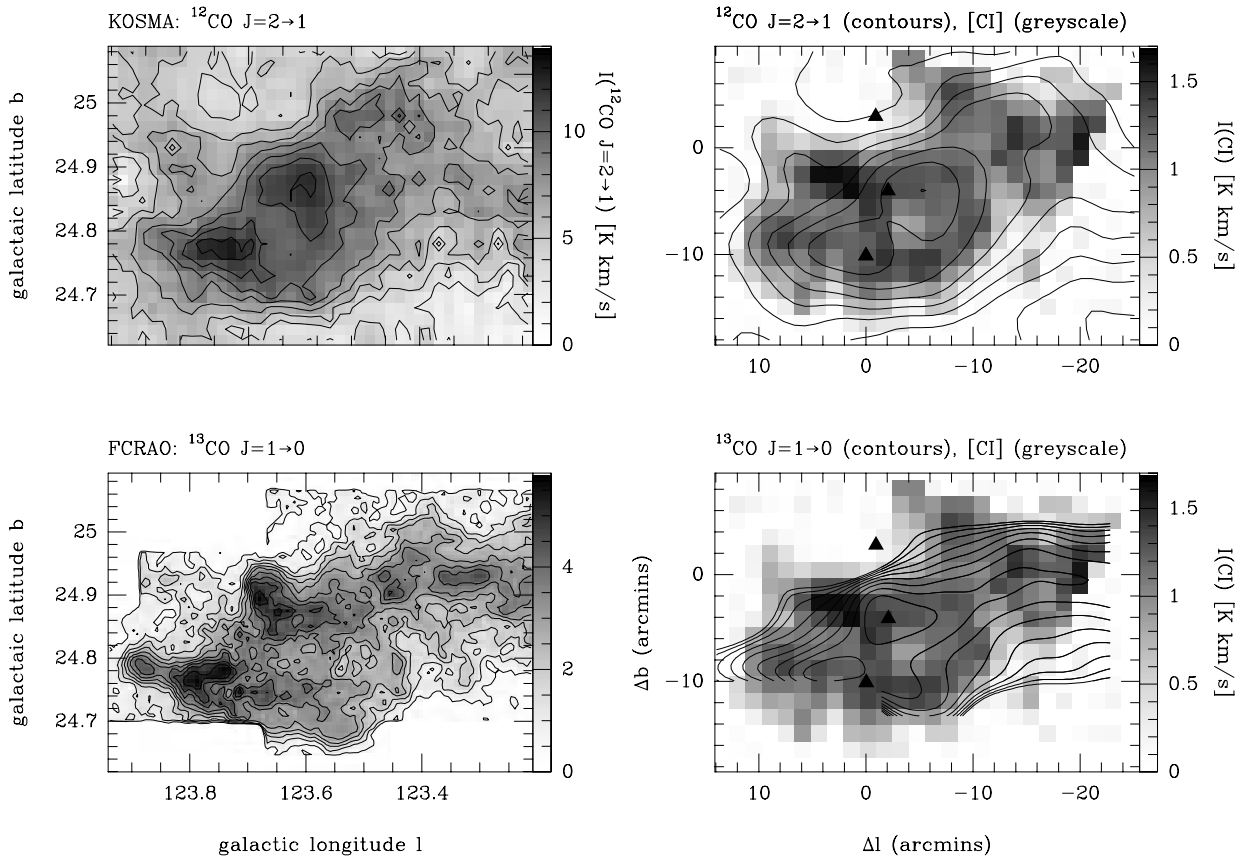


FIG. 1.—*Left*: ^{12}CO $J = 2 \rightarrow 1$ and ^{13}CO $J = 1 \rightarrow 0$ map observed with the KOSMA and FCRAO telescopes, respectively. *Gray scale*: Velocity-integrated intensity $I_{\rm peak} = \int T_{\rm mb}\, dv$. *Contours*: Peak intensity from 10% to 90%, in steps of 10% ($I_{\rm peak} = 13.5$ K km s^{-1} for ^{12}CO and 5.83 K km s^{-1} for ^{13}CO). *Right*: Overlay of the *SWAS* [C I] $^3P_1 \rightarrow {}^3P_0$ integrated intensity map (*gray scale*) with the ^{12}CO $J = 2 \rightarrow 1$ and ^{13}CO $J = 1 \rightarrow 0$ maps (*contours*). CO maps are smoothed to the angular resolution of the *SWAS* observations. *Contours*: $I_{\rm peak}$ of 20% to 90%, in 10% increments [$I_{\rm peak}(^{12}{\rm CO}) = 11.6$ K km s^{-1}, $I_{\rm peak}(^{13}{\rm CO}) = 4.2$ K km s^{-1}]. Coordinates are given relative to ($l = 123\overset{\circ}{.}68$, $b = 24\overset{\circ}{.}93$). *Filled triangles*: Positions of the line profiles shown in Fig. 2.

spectra obtained for two positions (270 and 473 minutes). The rms noise $\Delta T_{\rm mb}$ is smaller than 0.13 K per velocity channel (0.623 km s^{-1}) for 93% of the spectra, and the typical rms noise level is 0.09 K per channel. [C I] emission with a velocity-integrated intensity $I_{\rm C\,I} = \int T_{\rm mb}[{\rm C\ I}]\, dv$ larger than 0.45 K km s^{-1} ($\equiv 3\ \sigma$ limit) is detected for 56 of the 80 positions observed. The resulting velocity-integrated map is shown in the right panels of Figure 1. It is the first [C I] map observed for a high-latitude translucent cloud. The typical line peak temperature and integrated intensity observed toward regions with the brightest emission is $T_{\rm mb} = 0.65$ K and $I_{\rm C\,I} = 1.0$–1.6 K km s^{-1}, respectively. We note that *SWAS* allows for simultaneous observations of [C I], ^{13}CO $J = 5 \rightarrow 4$ at 550.9 GHz, O_2 at 487.2 GHz, and H_2O at 556.9 GHz; however, no emission is detected for the latter three transitions for an rms noise limit of $\Delta T_{\rm mb} \sim 26$ mK per velocity channel.

Complementary observations of the ^{12}CO $J = 1 \rightarrow 0$ and $J = 2 \rightarrow 1$ transitions made with the KOSMA 3 m telescope are available from Grossmann et al. (1990) and Bensch, Stutzki, & Ossenkopf (2001). In addition, observations of the ^{13}CO $J = 1 \rightarrow 0$ transition were made with the FCRAO 14 m telescope in 1999 December and of the ^{13}CO $J = 2 \rightarrow 1$ and ^{12}CO $J = 3 \rightarrow 2$ transitions with the KOSMA telescope in 1999 October–November and 2000 October. The CO maps cover at least 90% of the area mapped in the [C I], with the exception of the ^{13}CO $J = 2 \rightarrow 1$ map, which covers a smaller fraction of the cloud ($\sim$20%). A summary of the observations is given in Table 1. The velocity-integrated map of the ^{12}CO $J = 2 \rightarrow 1$, ^{13}CO $J = 1 \rightarrow 0$, and the [C I] $^3P_1 \rightarrow {}^3P_0$ transition is shown in Figure 1, and the line profiles for three representative positions are shown in Figure 2.

3. RESULTS

3.1. *Morphology of the* [C I] *Emission and Line Ratios*

Generally, the [C I] emission is spatially extended and follows the region with bright ^{12}CO emission. In fact, Figure 3 below shows that the observed spectra are consistent with a roughly constant ratio of the line-integrated flux densities of [C I] and both lower ^{12}CO transitions. In contrast, the ^{13}CO line flux density decreases more steeply from the emission peak toward the ambient cloud, and only a little intensity is found outside the 60% contour of the ^{12}CO $J = 2 \rightarrow 1$ map. A more detailed study of the spatial intensity distribution is difficult because of the limited signal-to-noise ratio of the [C I] data.

For a quantitative analysis of the spectra, we smoothed the CO data to the *SWAS* velocity resolution, in addition to the angular convolution and resampling of the data on the grid of the [C I] observations. We determined the line center and line width from a Gaussian fit to the observed line

TABLE 1
SPECTRAL LINE OBSERVATIONS TOWARD MCLD 123.5+24.9

Telescope	Transition	Position on the Map	Sampling	Main Beam FWHM	$B_{\rm eff}/F_{\rm eff}$	References[a]	Line Center $\langle v_0 \rangle$ (km s^{-1})	Line Width $\langle \Delta v \rangle$ (km s^{-1})
SWAS	[C I] $^3P_1 \rightarrow {}^3P_0$	80	3.′2	4.′3	0.9		-3.42 ± 0.51	2.38 ± 0.72
KOSMA	^{12}CO $J = 1 \rightarrow 0$	255	4.′0	3.′9	0.64/0.78[b]	1	-3.79 ± 0.31	2.47 ± 0.30
KOSMA	^{12}CO $J = 2 \rightarrow 1$	2976	1.′0	2.′0	0.70	2	-3.67 ± 0.39	2.42 ± 0.32
KOSMA[a]	^{12}CO $J = 3 \rightarrow 2$	1100	1.′0	1.′43	0.68		-3.71 ± 0.38	2.00 ± 0.38
FCRAO	^{13}CO $J = 1 \rightarrow 0$	10368	0.′37	0.′78	0.48	2	-3.65 ± 0.44	1.44 ± 0.32
KOSMA[c]	^{13}CO $J = 2 \rightarrow 1$	440	1.′0	1.′9	0.68		-3.60 ± 0.44	1.37 ± 0.33

[a] (1) Grossmann et al. 1990. (2) Bensch, Stutzki, & Ossenkopf 2001.
[b] The efficiency of $B_{\rm eff}/F_{\rm eff} = 0.64$ applies to observations made before a readjustment of the telescope panels 1991 November.
[c] Observations made with the new KOSMA telescope.

profiles and corrected for the velocity resolution of the spectrometer. For each transition, the average and rms of the thus-derived quantities are listed in Table 1. While the line width of the [C I] and ^{12}CO spectra are very similar ($\sim$2.4 km s^{-1}), significantly smaller line widths are detected for the ^{13}CO transitions ($\sim$1.4 km s^{-1}). This is also evident from the line profiles shown in Figure 2. The similarities in the spatial distribution and the line profile of the [C I] and ^{12}CO emission suggest that the emission from both tracers originates in the same volume of space and therefore has similar excitation conditions.

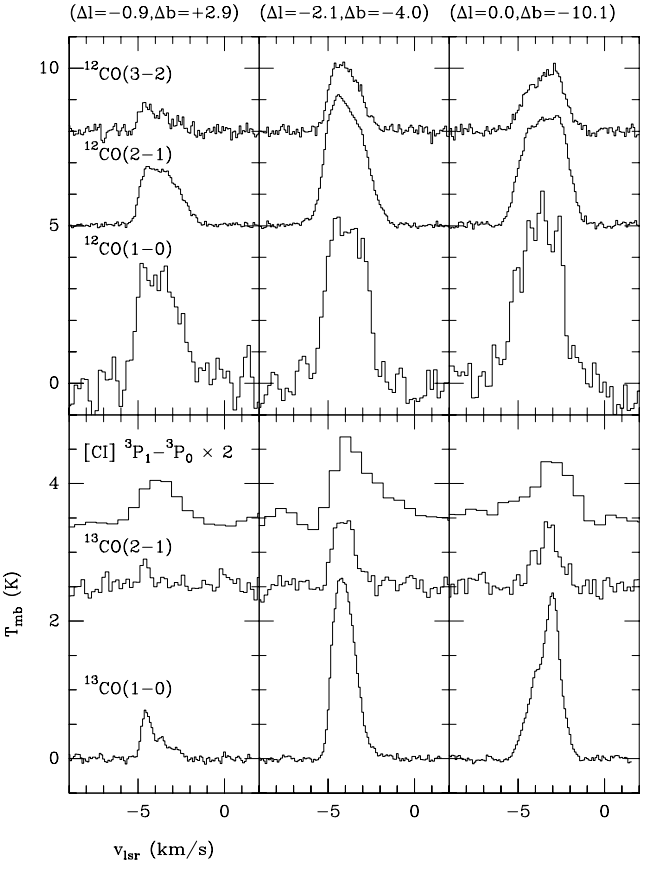


FIG. 2.—Line profiles of ^{12}CO, ^{13}CO, and [C I] $^3P_1 \rightarrow {}^3P_0$ for three representative positions. *Left column*: Spectra are centered on a position with only weak ^{13}CO emission, marked by the uppermost of the triangles in Fig. 1. *Middle column*: Spectra observed toward one of the cores visible in high-density tracers (^{13}CO peak). *Right column*: Centered on a local maximum of the ^{12}CO emission. All spectra have been smoothed to the *SWAS* angular resolution of 4.′3.

The same result was noted for other diffuse and translucent molecular clouds (Keene, Blake, & Phillips 1987; Stark & van Dishoeck 1994; Heithausen et al. 2001). In contrast, Ingalls, Bania, & Jackson (1994) and Stark et al. (1996) find a close correlation between [C I] and ^{13}CO emission in their studies of translucent clouds and cloud edges. The reason for the contrasting results is not clear; however, it might be related to the somewhat larger column densities and thus larger optical depths of the ^{13}CO transitions that are probed toward the clouds in the latter studies.

In the following, we determine the integrated intensity ratio observed for the [C I], ^{12}CO, and ^{13}CO transitions. This will serve as the basis for a quantitative comparison of the line cooling by neutral carbon and CO and for a comparison to PDR models. For this purpose, we determine the line integrated intensity, $I = \int T_{\rm mb}\, dv$ (K km s^{-1}), and the line flux density, $F = 2\, k\, \nu^3\, c^{-3}\, I$ (ergs s^{-1} cm^{-2} sr^{-1}), for each spectrum. The ratio of the line flux density is referred to as R(C I/^{12}CO, J_u–J_l) = F(C I, $^3P_1 \rightarrow {}^3P_0$)/$F$(^{12}CO, J_u–J_l) for the ^{12}CO $J : J_u \rightarrow J_l$ transition and R(C I/^{13}CO, J_u–J_l) for the corresponding transition of the rarer isotopomer. Figure 3 shows the observed ratios for positions with detected [C I] emission as a function of the ^{12}CO (^{13}CO) line flux density.

The ratio R(C I/^{13}CO, 1–0) scatters over a wide range and significantly increases for regions with weak ^{13}CO $J = 1 \rightarrow 0$ emission, and a similar trend is observed for the R(C I/^{13}CO, 2–1) ratio. The corresponding ratio for [C I] and both lower ^{12}CO rotational transitions, in contrast, remains constant. (The scatter of the individual data points, however, increases for small $F_{^{12}\rm CO}$, due to the smaller signal-to-noise ratio of the spectra.) For both ^{12}CO transitions, the average ratio is consistent with the slope derived from a linear least-squares fit to the [C I] and the ^{12}CO line flux density. Only for the R(C I/^{12}CO, 3–2) ratio is an increase toward small F(^{12}CO, 3–2) obvious. A summary of the observed line ratios is given in Table 3.

3.2. *Line Excitation and Neutral Carbon Column Density*

For regions bright in CO, the excitation conditions for both lower ^{12}CO transitions are close to LTE with an excitation temperature of $T_{\rm ex} = 7.5$–8 K and a beam filling factor of the emission close to unity. The large optical depths of the ^{12}CO lines are indicated by the line profiles, which are flat-topped toward many positions. The lower limit of the excitation temperature derived from the line peak intensities is 7.9 K (^{12}CO $J = 1 \rightarrow 0$), 8.2 K (^{12}CO $J = 2 \rightarrow 1$), and

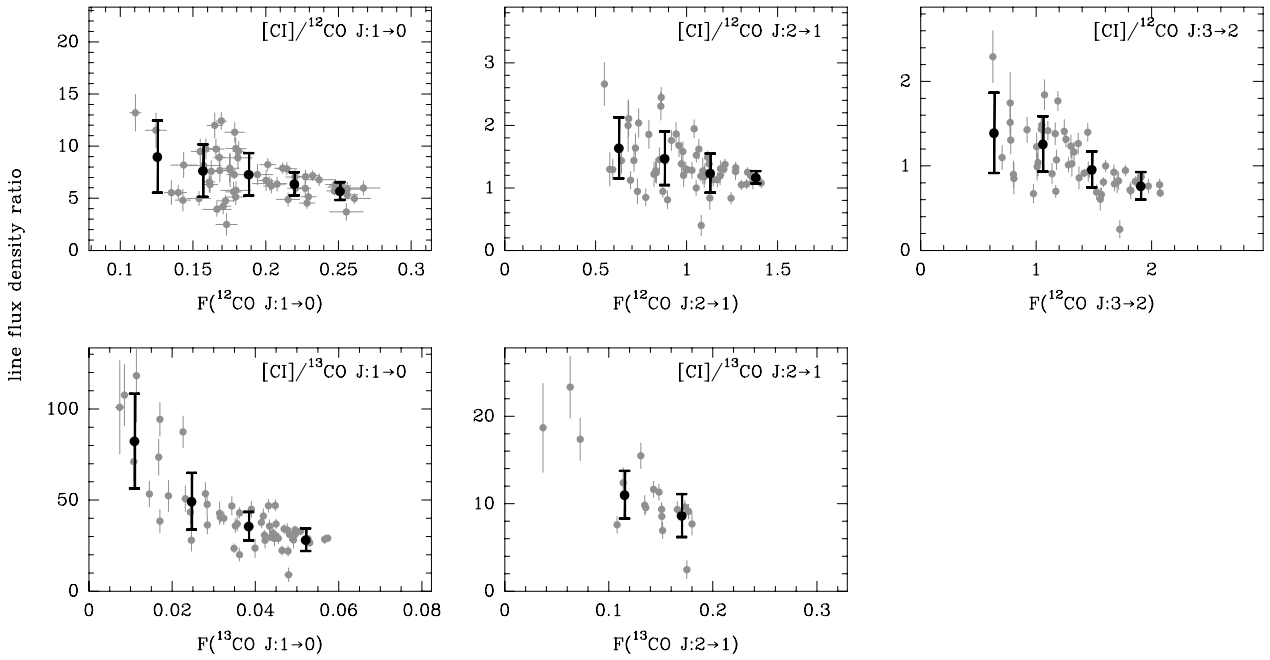


FIG. 3.—Line flux density ratio of [C I] to CO as a function of the CO line flux density for the three ^{12}CO and both ^{13}CO rotational transitions (F in units of 10^{-7} ergs s^{-1} cm^{-2} sr^{-1}). *Small gray symbols*: Ratio determined for the individual positions. *Large filled circles with error bars*: Average and rms of the ratios in equally spaced bins. The grand average and rms of the ratios are listed in Table 3.

7.3 K for ^{12}CO $J = 3 \rightarrow 2$. (Note that the Rayleigh-Jeans correction is substantial for the low temperatures and high frequencies involved.) This is consistent with the excitation temperature of $T_{\rm ex} = 7.2^{+1.3}_{-1.0}$ derived from the ratio of the line-integrated intensity of both lower ^{12}CO transitions, $I_{^{12}\rm CO(2-1)}/I_{^{12}\rm CO(1-0)} = 0.65 \pm 0.05$. Even the ^{12}CO $J = 3 \rightarrow 2$ transition is close to being thermalized for regions with bright CO emission. The ^{12}CO $J = 3 \rightarrow 2$ to $J = 2 \rightarrow 1$ ratio of 0.64 ± 0.02 derived from a linear fit for channels with $T_{\rm mb}(^{12}\rm CO\ J = 2 \rightarrow 1) > 2$ K suggests that $T_{\rm ex} = 7.6 \pm 0.5$. This also argues for densities around or larger than the critical density of the ^{12}CO $J = 3 \rightarrow 2$ transition ($\sim 5 \times 10^4$ cm^{-3}) for regions with bright CO emission, including an appropriate correction for line trapping at moderate optical depths.

We derived the total CO column densities from the ^{13}CO $J = 1 \rightarrow 0$ observations using standard LTE equations (Rohlfs & Wilson 2000), $T_{\rm ex} = 8$ K, and assuming a [^{12}CO]/[^{13}CO] abundance ratio of 65. All column densities have been corrected for the line optical depth derived from the observed peak temperature and assuming a Gaussian line profile. The CO column densities on the angular resolution of the *SWAS* observations range from $N_{\rm CO} \sim 0.3 \times 10^{17}$ cm^{-2} for regions with weak emission to $N_{\rm CO} \sim 3 \times 10^{17}$ cm^{-2} toward the ^{13}CO cores.

Typical [C I] line peak temperature are between 0.3 and 0.55 K for positions where [C I] is detected, with a maximum of 0.65 K. This is significantly smaller than the $T_{\rm mb,\ peak} = 1.3$ K expected for optically thick emission and LTE excitation conditions with $T_{\rm ex} \sim 8$ K. If LTE applies, the [C I] line peak temperature suggests an optical depth of smaller than 0.65 and a neutral carbon column density ranging from $N_{\rm C} = 10^{17}$ cm^{-2} for the region with the strongest emission to $N_{\rm C} = 2.5 \times 10^{16}$ cm^{-2}, the 3 σ detection limit of our data set. The resulting C to CO abundance ratio varies between 0.2 for the ^{13}CO cores to 1.1 for regions with weak ^{13}CO emission (Fig. 4).

We note that the excitation temperature of [C I] cannot be below 7 K, unless we assume that the total abundance of carbon in the gas phase is enhanced in MCLD 123.5+24.9. The optical depth determined from the observed line peak intensities are of the order of unity for $T_{\rm ex} = 7$ K and rapidly increases if smaller temperatures are assumed. The total column density of neutral carbon and CO then is $N_{\rm C} + N_{\rm CO} \gtrsim 3 \times 10^{17}$ cm^{-2}, even for regions with $A_V \lesssim 1$, corresponding to $N_{\rm H}(\rm tot) = N(\rm H) + 2N(\rm H_2) \lesssim 1.9 \times 10^{21}$

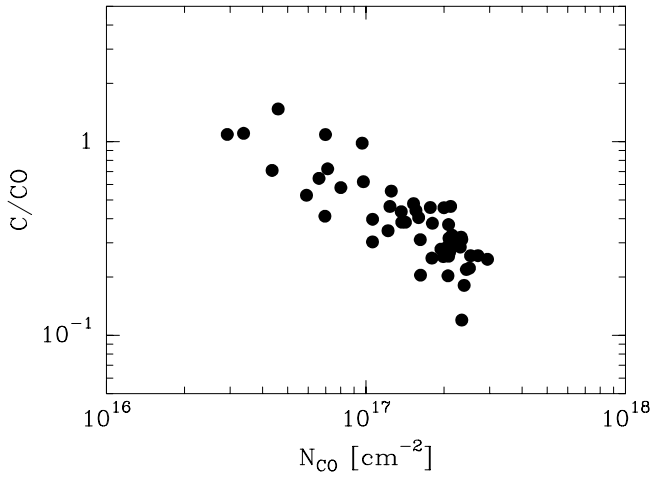


FIG. 4.—Column density ratio of C to CO in MCLD 123.5+24.9 for the positions with detected [C I] emission. Column densities were determined from the [C I] $^3P_1 \rightarrow {}^3P_0$ and ^{13}CO $J = 1 \rightarrow 0$ spectra observed for each position, assuming LTE and homogeneous excitation conditions with $T_{\rm ex} = 8$ K.

cm^{-2}. Assuming a lower excitation temperature for the [C I] transition therefore results in a total carbon abundance of larger than 3×10^{-4} per hydrogen particle, not accounting for the ionized carbon that is expected to be abundant in the cold neutral envelope surrounding the cloud and further increases the carbon abundance. Higher [C I] excitation temperatures than the $T_{ex} = 7.5$–8 K derived from the LTE analysis are not excluded. If we assume $T_{ex} \gtrsim 10$ K, the optical depth derived for the [C I] line peak is smaller than 0.25. This would give a C to CO column density ratio of $N_C/N_{CO} \lesssim 0.4$.

We consider subthermal excitation of the [C I] transition as unlikely. This would require that the [C I] and the ^{12}CO emission originates from two distinct volumes of spaces of different density, $n \lesssim 10^3$ and $n \gtrsim 10^4$ cm^{-3}, where the upper (lower) limit is given by the critical density[4] of the [C I] $^3P_1 \rightarrow {}^3P_0$ and ^{12}CO $J = 2 \rightarrow 1$ transitions, respectively. The similarities in the line profiles and the constant [C I] to ^{12}CO liner ratio argue against this case.

We note that the assumption of homogeneous excitation conditions for the observed tracers are likely to overestimate the C/CO abundance ratio. The ratio of the ^{13}CO $J = 2 \rightarrow 1$ to $J = 1 \rightarrow 0$ integrated intensity is significantly smaller than expected for the excitation temperature suggested by the ^{12}CO data. This might be due to a temperature gradient from the cloud surface to the interior, with the ^{13}CO transitions tracing the colder regions at greater depths, whereas [C I] and the optically thick ^{12}CO emission originates in the warmer cloud surface. This is not an exceptional result, as temperature gradients have been invoked to model multiline data sets for numerous molecular clouds (Castets et al. 1990; Kramer, Stutzki, & Winewisser 1996), including high-latitude translucent clouds (Schreiber et al. 1993), and naturally occur on externally heated PDR surfaces of clumps (Gierens, Stutzki, & Winewisser 1992; Störzer, Stutzki, & Sternberg 1996). The CO column densities derived above therefore probably underestimate the true CO column density, and the C/CO ratios shown in Figure 4 should be considered as upper limits. Moreover, the ^{13}CO to ^{12}CO abundance ratio might deviate from the isotope ratio because of processes such as photodissociation (van Dishoeck & Black 1988) and fractionation reactions (Watson, Anicich, & Huntress 1976; Smith & Adams 1980), both of which potentially are important to low-A_V environments. In any case, the neutral carbon and CO column densities derived from [C I] and ^{13}CO observations assuming homogeneous clouds with constant abundances and excitation conditions have to be treated with caution.

3.3. *Line Cooling*

For MCLD 123.5+24.9, the cooling by the ^{12}CO rotational transitions is larger than by the [C I] fine-structure transitions (Table 2). The line flux density for ^{12}CO $J = 3 \rightarrow 2$ is 0.5×10^{-7} ergs s^{-1} cm^{-2} sr^{-1} for the region with the weakest ^{12}CO emission and increases to 2×10^{-7} ergs s^{-1} cm^{-2} sr^{-1} for the CO peak in our map. The $J = 2 \rightarrow 1$ line flux density is slightly smaller than for the $J = 3 \rightarrow 2$ transition, $(0.5$–$1.3) \times 10^{-7}$ ergs s^{-1} cm^{-2} sr^{-1}, whereas the flux density of the $J = 1 \rightarrow 0$ is more than $\sim$6 times smaller. Thus, the total line cooling by the three lowest CO rotational transitions is $(1.3$–$3.5) \times 10^{-7}$ ergs s^{-1} cm^{-2} sr^{-1}. For the same regions, the line flux density of the [C I] $^3P_1 \rightarrow {}^3P_0$ transition is $(0.7$–$1.7) \times 10^{-7}$ ergs s^{-1} cm^{-2} sr^{-1}. The $^3P_2 \rightarrow {}^3P_1$ transition contributes by no more than 0.3×10^{-7} ergs s^{-1} cm^{-2} sr^{-1}, if we assume $T_{ex} = 8$ K and the neutral carbon column densities derived above. From the line ratios listed in the left column of Table 3, we derive an upper limit to the ratio of the gas cooling by [C I] $^3P_1 \rightarrow {}^3P_0$ to the CO cooling of $\Lambda_C/\Lambda_{CO} = 0.55$, if we assume that the contribution by higher CO transitions is negligible. The latter critically depends on the gas density. For instance, the CO cooling in a cloud with $T_{ex} = 8$ K, $n \geq 5 \times 10^5$ cm^{-3}, and a column density of $N_{CO} \leq 2 \times 10^{17}$ cm^{-2} is dominated by the $J = 4 \rightarrow 3$ transition, and by the $J = 3 \rightarrow 2$ transition for $n \lesssim 5 \times 10^5$ cm^{-3} (LTE assumed).

We note that even for translucent clouds and weak ambient FUV field, the cooling can be dominated by the [C II] $^2P_{3/2} \rightarrow {}^2P_{1/2}$ fine-structure transition of ionized carbon. The typical [C II] line flux density observed toward high-latitude translucent clouds of $(2$–$20) \times 10^{-7}$ ergs s^{-1} cm^{-2} sr^{-1} (cf. Matsuhara et al. 1997; Timmermann, Köster, & Stutzki 1998) is larger than those of the [C I] and CO flux densities observed here. No [C II] observations are, however, available for MCLD 123.5+24.9.

TABLE 2

MCLD 123.5+24.9: Observed Line Flux Toward Three Representative Positions[a]

Species Transition	Position 1 (−0.′9, 2.′9)	Position 2 (0.′5, −1.′7)	Position 3 (0.′0, −10.′1)
C I $^3P_1 \rightarrow {}^3P_0$	0.767 ± 0.085	1.300 ± 0.055	1.410 ± 0.100
^{12}CO $J = 1 \rightarrow 0$	0.154 ± 0.002	0.176 ± 0.003	0.247 ± 0.005
^{12}CO $J = 2 \rightarrow 1$	0.593 ± 0.004	1.003 ± 0.005	1.330 ± 0.007
^{12}CO $J = 3 \rightarrow 2$	0.602 ± 0.025	1.416 ± 0.024	2.075 ± 0.022
^{13}CO $J = 1 \rightarrow 0$	0.011 ± 0.001	0.044 ± 0.001	0.053 ± 0.001
^{13}CO $J = 2 \rightarrow 1$	0.042 ± 0.008	0.136 ± 0.008	0.151 ± 0.007
$I(\text{C I}) / \sum \text{I(CO)}$	0.55 ± 0.07	0.47 ± 0.02	0.37 ± 0.19

[a] $F = 2\ k\ \nu^3\ c^{-3}\ \int T_{mb}\ dv$ in units of 10^{-7} ergs s^{-1} cm^{-1} sr^{-1}.

4. PDR MODELING

The translucent cloud MCLD 123.5+24.9 is embedded in the mean interstellar radiation field. Though weak, the interstellar FUV field heats the cloud surface and chemical reactions induced by the external FUV radiation are

TABLE 3

Line Flux Density Ratios

Ratio (1)	Average ± rms (2)	90% Range[a] (3)	Literature[b] (4)
$R(\text{C I}/^{12}CO,\ 1$–$0)$	7.00 ± 2.26	1.17–11.4	7.8–27
$R(\text{C I}/^{12}CO,\ 2$–$1)$	1.37 ± 0.41	0.83–2.14	1.0–5.4
$R(\text{C I}/^{12}CO,\ 3$–$2)$	1.06 ± 0.37	0.63–1.76	1.0–2.3
$R(\text{C I}/^{13}CO,\ 1$–$0)$	42.7 ± 22.3	22.2–107	70–620
$R(\text{C I}/^{13}CO,\ 2$–$1)$	10.5 ± 3.9	6.90–17.4	7.8–14.5

[a] Observed ratios are within the range of 90%.

[b] Range derived from observations published in the literature: Keene, Blake, & Phillips 1987; Stark & van Dishoeck 1994; Ingalls, Bania, & Jackson 1994; Stark et al. 1996; Ingalls et al. 1997; Heithausen et al. 2001 and references therein.

[4] For collisions with H_2.

expected to govern the formation and excitation of neutral carbon. In the following, we examine whether or not PDR models provide a consistent description for the emission observed in the [C I] and CO transitions. We employ the PDR model for a spherical symmetric geometry by Störzer, Stutzki, & Sternberg (1996). The clumps have a power-law density profile $n(r) = n_s(r/r_c)^{-1.5}$ for $r_c \leq r \leq 0.2\ r_c$ and a constant density of $n(r) = (0.2)^{-1.5}\ n_s$ in the clump center ($r \leq 0.2\ r_c$). Here $M_{\rm cl}$, r_c, and n_s denote the total mass of the clump, the clump radius, and the density at the clump surface. The average clump density is approximately twice the clump surface density, $\langle n_{\rm cl}\rangle \approx 2n_s$. The chemical network of the PDR code includes ^{13}C and the appropriate chemical reactions important to the formation and destruction of ^{13}CO (fractionation reactions and isotope-selective photodissociation). In addition, we extended the network by sulfur-bearing species and additional hydrogen-carbon molecules (CH_n and CH^+_{n+1}, where $2 \leq n \leq 4$). Both groups of species are important for the formation and removal of neutral carbon in PDRs (Tielens & Hollenbach 1985; Sternberg & Dalgarno 1995). The initial gas-phase elemental abundances were taken from Savage & Sembach (1996).

4.1. *Clumps in a Weak UV Field*

For the PDR simulations, we use an external FUV field of $\chi = 1.0\chi_0$ and compare these results to PDR models with 0.5 and 2 times χ_0. We consider $0.5\chi_0$ to be a lower limit of the FUV strength at the location of the cloud on the basis of results by Bernard et al. (1999). For each χ, we run a grid of 8×8 models with a clump mass $10^{-5}\ M_\odot \leq M_{\rm cl} \leq 100\ M_\odot$ and an average clump density of $600\ {\rm cm}^{-3} \leq \langle n_{\rm cl}\rangle \leq 2 \times 10^6\ {\rm cm}^{-3}$ (Fig. 5, *left panel*). The clump-averaged line flux densities are determined for [C I] and the ^{12}CO, ^{13}CO rotational transitions using the radiative transfer code by Gierens et al. (1992). Figure 5 (*right panel*) and Figure 6 compare the observations and the PDR models, showing $F_{\rm C\,I}$ and the [C I] to CO flux density ratios, respectively. For most models, the projected clump diameter at the distance of MCLD 123.5+24.9 is much smaller than the *SWAS* main beam FWHM, and the emission from a large number of clumps is sampled for each line of sight (Fig. 5, *left panel, bold dashed lines*). The line ratios therefore provide quantities that do not depend on the beam filling factor of the clumps, in contrast to the total line flux densities.

For clumps with a low visual extinction ($A_V \lesssim 0.5$), the [C I] emission is optically thin and the line flux density $F_{\rm C\,I}$ scales with the total carbon column density of the clump. In this regime, the chemistry throughout the whole clump is dominated by the external FUV field and the C abundance decreases with the clump-averaged A_V. In addition, $F_{\rm C\,I}$ decreases for clumps with densities smaller than the critical density of the [C I] $^3P_1 \rightarrow {}^3P_0$ transition. For $\langle n_{\rm cl}\rangle \gtrsim 10^5\ {\rm cm}^{-3}$, the neutral carbon is confined to a thin surface layer of the clump, and the total carbon column density in the clump slightly decreases. The clump-averaged [C I] line flux density does not depend on the total clump mass but on the temperature structure close to the clump surface. The gas temperature rapidly drops below 10 K within a thin surface layer, while the abundance of neutral carbon decreases more gradually. The small decrease in the [C I] intensity therefore largely reflects the steep temperature profile close to the surface for clumps with large densities. The smaller gas temperatures for higher densities result from the contribution of the higher CO rotational transitions to the gas cooling ($J = 5 \rightarrow 4$ and $J = 4 \rightarrow 3$ with $n_{\rm crit.} \gtrsim 10^5\ {\rm cm}^{-3}$).

The emission of the three lowest ^{12}CO rotational transition varies with the clump-averaged visual extinction. Photodissociation of CO dominates throughout the clump for visual extinction of $A_V \lesssim 2$, and the clump-averaged ^{12}CO line intensities rapidly decrease for small A_V. For clumps with low densities, the observed line is further reduced due to subthermal line excitation. This is more noticeable for the $J = 3 \rightarrow 2$ and $J = 2 \rightarrow 1$

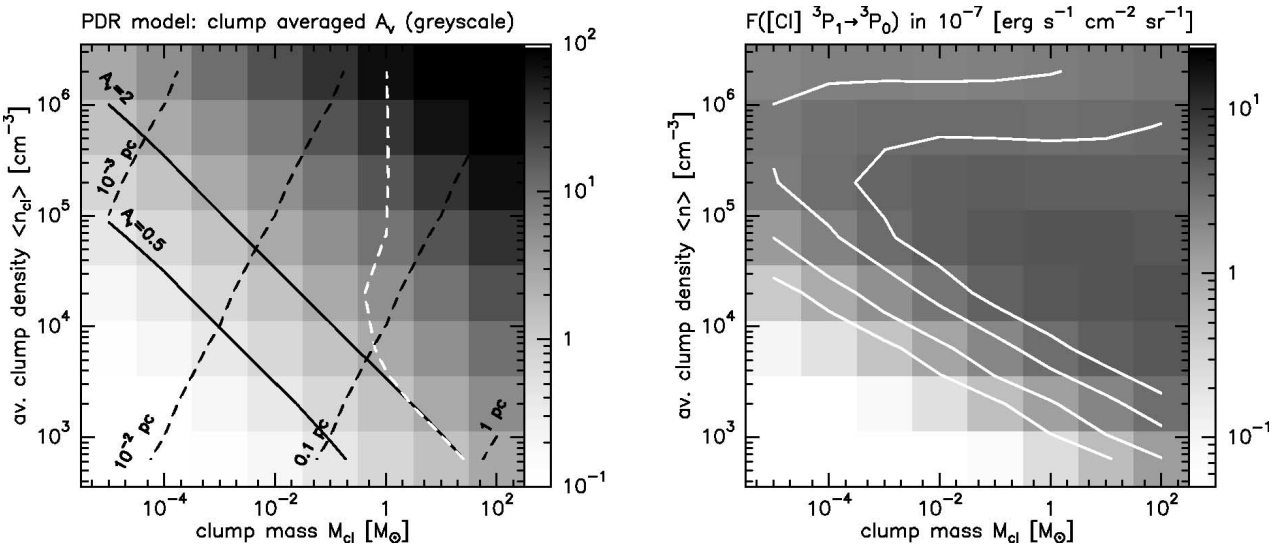


FIG. 5.—PDR model for spherical symmetric geometry. *Left panel*: Clump averaged A_V (*gray scale*) as a function of clump mass and clump density. *Solid contours*: $A_V = 0.5$ and 2.0, bracketing the range of extinction applicable for MCLD 123.5+24.9 at an angular resolution of 5′. *Dashed lines*: Clumps with the same radius and range from 10^{-3} (*upper left*) to 1 pc (*lower right*). *White dashed line*: Clumps to the right of and above this line are excluded on the basis of the observed visual extinction ($A_V \lesssim 2$) if viewed with an 4.′3 beam at a distance of 150 pc. *Right panel*: Clump averaged [C I] $^3P_1 \rightarrow {}^3P_0$ line flux density ($\chi = 1.0\ \chi_0$). *Contours*: Line flux densities of 0.5, 1, 2, and 3×10^{-7} ergs cm^{-2} s^{-1} sr^{-1}.

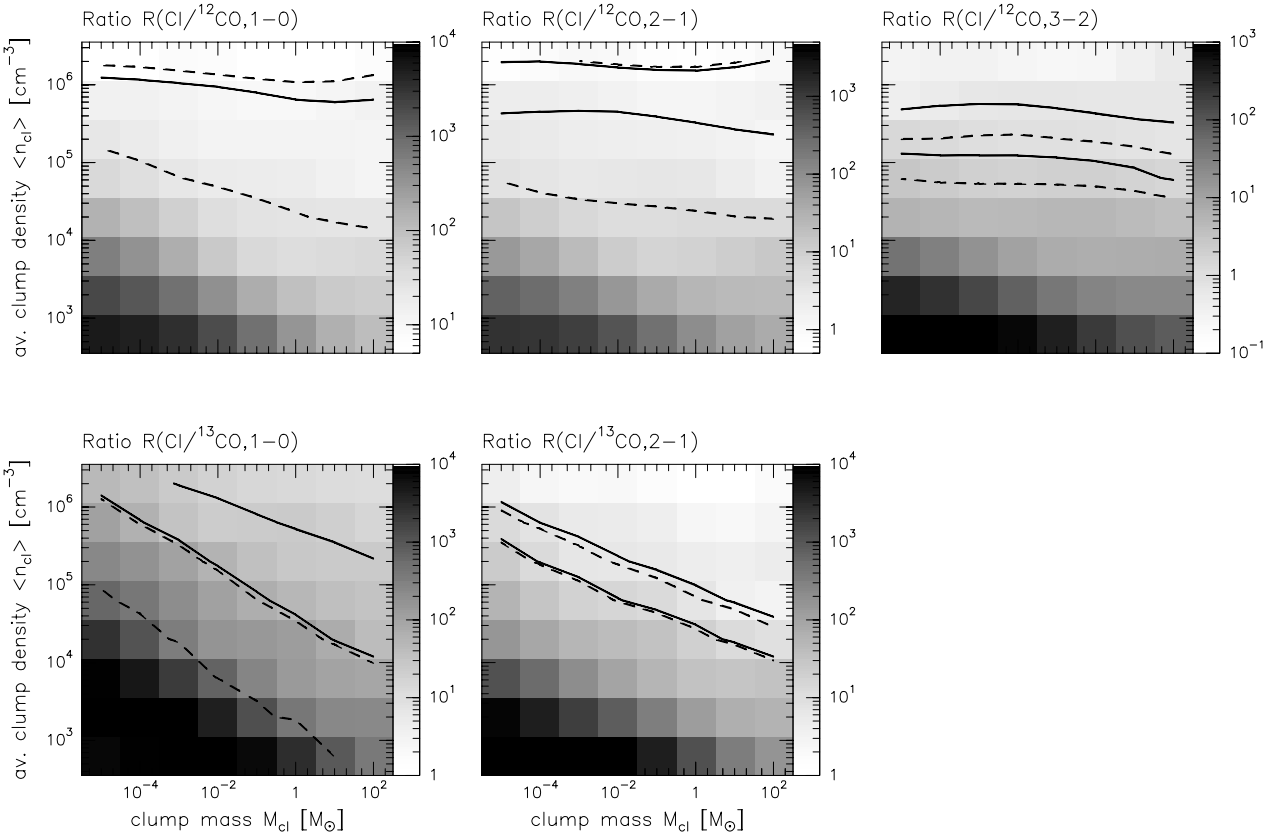


FIG. 6.—Results from the PDR model for an external FUV field with $\chi = 1 \times \chi_0$. *Gray scale*: Ratio of the clump-averaged line flux of [C I] and CO rotational transition shown as a function of the total clump mass and the average clump density. The particular ratio is shown at the top of each panel. *Solid lines*: $\pm 1\ \sigma$ range of the average line ratio in MCLD 123.5+24.9, listed in column (2) of Table 3. *Dashed lines*: Range typically observed toward other translucent and diffuse clouds, listed in the last column of Table 3.

transitions because of their larger critical density (5×10^4 cm^{-3} and 10^4 cm^{-3}). For clumps with a large A_V, the ^{12}CO emission rapidly becomes optically thick in the line center. The integrated intensity therefore increases much more slowly with A_V, as the optical depth even in the line wings becomes significant, effectively broadening the line profile. Together with the weak dependence of the [C I] intensity for clumps with larger densities, this results in a similarly weak dependence of the [C I] to ^{12}CO line ratios in this range (Fig. 6, *top panels*). In this regime, the line ratio essentially probes the temperature close to the clump surface.

Similar to ^{12}CO, the ^{13}CO line integrated intensity of the low-J transitions increases from low to high clump-averaged A_V. However, the intensity shows a significant increase even for the largest A_V because of the smaller optical depth for the transitions of the rarer isotopomer. As a result, the [C I] to ^{13}CO line ratios increase with clump mass, even for the largest densities in our simulations (Fig. 6, *bottom panels*). For the lowest A_V, the velocity-integrated intensity rapidly diminishes. Here, isotope-selective photodissociation results in a stronger depletion of ^{13}CO for these models than for the more abundant ^{12}CO. This is reflected by the steeply rising [C I] to ^{13}CO line ratio.

The observed [C I] to ^{12}CO line ratios constrain the PDR model to high-clump densities, even for regions with weak CO emission. R(C I, ^{12}CO, 3–2) gives densities of the order of a few times 10^5 cm^{-3}, whereas R(C I, ^{12}CO, 1–0) suggests even higher densities exceeding 10^6 cm^{-3}. The clump mass cannot be ascertained by the observations.

The [C I] to ^{13}CO line-integrated intensity, in contrast, shows larger variations for clumps of different mass, and together with the ^{12}CO observations, constrains the PDR models to clumps with $M < 0.1\ M_\odot$. The large scatter in the observed ratio for regions with weak ^{13}CO emission, however, translates to a correspondingly wide range of clump mass and density. We note that the PDR model for these clumps predicts a [C I] $^3P_1 \rightarrow {}^3P_0$ line flux density that is larger than the observed flux densities by a factor of 1.5–3 (Fig. 5, *right panel*).

The reduction of the FUV field strength by 50% results in smaller [C I] to CO line ratios and, thus, in a smaller density for a given line ratio. Conversely, an increased FUV intensity results in higher densities for the observed line ratios. However, the comparison of the PDR results for $\chi = 0.5\chi_0$ to the observed R(C I/^{12}CO, 1–0) and R(C I/^{12}CO, 2–1) gives densities that are smaller by less than a factor of 3. For the R(C I/^{12}CO, 3–2), similar densities are obtained for $\chi = 0.5\chi_0$ and $1\chi_0$. Thus, even in the case of a reduced FUV intensity at the location of MCLD 123.5+24.9, the PDR model suggests densities exceeding 10^5 cm^{-3}.

4.2. *Clumps Embedded in an Interclump Medium*

In the following, we examine the influence of a possible interclump medium on the emission and the line ratios. For

this purpose, we assume that the dense clumps are embedded in an interclump gas of density $n_{ic} = 10^{2.5}$ cm^{-3}. The total column density of a interclump medium is $A_V < 1$, if we assume that more than 50% of the gas is confined in dense clumps. (Recall that the total visual extinction observed toward MCLD 123.5+24.9 is $A_V = 1$–2.) Thus, the clumps are shielded by a gas column density of $N_H(\mathrm{tot}) = N(\mathrm{H}) + 2N(\mathrm{H_2}) < 9.4 \times 10^{20}$, which corresponds to $A_V < 0.5$.

The contribution of such an interclump medium to the observed [C I] emission is insignificant. For an estimate, we use spherical PDR models with a constant volume density of $n = 10^{2.5}$ cm^{-3} and a column density of $N_H(\mathrm{tot}) = 9.4 \times 10^{20}$ cm^{-2} from the clump surface to the center. For these clumps, most of the carbon is singly ionized: $n_{C^+} \gg n_C \gg n_{CO}$. Assuming that the angular extent of the emission is much larger than the *SWAS* main beam, an upper limit of the [C I] $^3P_1 \rightarrow {}^3P_0$ line flux density is 3.7×10^{-8}, the flux density emerging for a pencil beam toward the clump center. For $N(\mathrm{tot}) = 4.7 \times 10^{20}$ cm^{-2}, the [C I] flux density is 1.0×10^{-8} ergs s^{-1} cm^{-2} sr^{-1}. This is only ~15% (5%, respectively) of the observed [C I] line flux density. For the CO rotational transitions, the line flux densities are more than 3 orders of magnitude below the observations.

The line flux density predicted by the PDR model for the $^2P_{3/2} \rightarrow {}^2P_{1/2}$ transition of ionized carbon is $F_{C\,II} \sim 2 \times 10^{-6}$ ergs s^{-1} cm^{-2} sr^{-1}. This is well within the sensitivity range of future space and airborne observatories such as *Herschel* and the *Stratospheric Observatory For Infrared Astronomy* (*SOFIA*). For example, an integration time of ~7 minutes is needed for a 4 σ detection of this [C II] line with a spectral resolution of 1 km s^{-2} using GREAT, a first-generation heterodyne receiver currently under construction for *SOFIA*.

Even though the total column density is small and contribution to the observed [C I] and CO line flux density is negligible, the H_2 in the interclump gas can provide an efficient shielding for the CO in the embedded clumps against photodissociation. This results from the line absorption of the FUV photons by molecular hydrogen at frequencies which overlap with the CO line transitions leading to a dissociation of the molecule. *Note that for this reason, the presence of a preshielding* H_2 *column density is not equivalent to a general reduction of the ambient FUV field,* $\chi < \chi_0$. For a simulation, we use spherical clumps with the same parameters as in § 4.1 but, this time, assume that the clumps are embedded in an interclump gas. This is implemented by assuming a preshielding column density of H_2 and CO, $N_{ic}(H_2)$ and $N_{ic}(CO)$, with $N_{ic}(CO)$ being a function of $N_{ic}(H_2)$ (Köster 1998). We choose a clump mass of $M_{cl} = 0.1\ M_\odot$ and consider models with densities in the range $2 \times 10^3 \leq \langle n_{cl} \rangle \leq 2 \times 10^6$ cm^{-3} and H_2 preshielding column densities of $0 \leq N_{ic}(H_2) \leq 1 \times 10^{21}$ cm^{-2}. Note that we use a simplified approach here as we do not consider the emission from the interclump medium and the radiative transfer of the clump emission through the interclump medium. Figure 7 shows the clump averaged [C I]/CO line ratios and the [C I] line flux density. A comparison to the observed line ratios suggests gas densities of 10^4 cm^{-3} for the clumps in an interclump medium with $N_{ic}(H_2) = (0.5\text{–}1) \times 10^{20}$ cm^{-2}. This is significantly lower than the densities derived above for clumps with no preshielding.

5. DISCUSSION

5.1. *Ubiquitous Dense Gas in Translucent Clouds?*

The comparison of the observed line flux density ratios with the spherical PDR model with no preshielding interclump medium suggests high densities for the line-emitting regions. The low [C I] to low-J ^{12}CO ratios, in particular, imply densities in excess of 10^6 cm^{-3}. High densities of $n \gtrsim 10^5$ cm^{-3} are indeed found at angular scales $\lesssim 1'$ ($l \lesssim 0.04$ pc) for at least one of the cores in MCLD 123.5+24.9 (§ 2.1). The constancy of the observed flux density ratios at the angular resolution of the *SWAS* and for regions with weak CO emission, however, would argue for similar high densities *throughout* the cloud, which we consider as unlikely. Additional evidence for spatially extended high-density gas in MCLD 123.5+24.9 is not available, but high densities are also not strictly ruled out by observations.

The emission of tracers with high critical density is confined to the cores, and the line intensity rapidly drops below the detection limit for offsets much larger than the core radius. Lower densities for the gas not associated with the core are suggested by the studies of Falgarone et al (1998). They find typical densities of a few times 10^3 cm^{-3} for gas with weak ^{13}CO emission. This result is supported by the analysis of the ^{12}CO $J = 3 \rightarrow 2$ to $J = 2 \rightarrow 1$ ratio in § 3.2, which argues for a lower gas density ($n \lesssim 5 \times 10^4$ cm^{-3}) for regions offset from the ^{13}CO peak.

In addition, the ubiquitous gas with a high density would have a very small volume filling factor. The average column density of $N(H_2) \sim 1.3 \times 10^{21}$ cm^{-2} toward MCLD 123.5+24.9 translates to a mass of 0.6 $M_\odot$ per *SWAS* beam. For $\mathcal{N}$ clumps with a density $n = 10^{5.5}$ cm^{-3} in the beam, the clump mass and radius is $M_{cl} = 0.6\ \mathcal{N}^{-1}\ M_\odot$ and $r_{cl} = 0.025\ \mathcal{N}^{-1/3}$ pc. This implies a volume filling factor for the clumps of smaller than $(r_{cl}/r_{SWAS})^3 \approx 0.02/\mathcal{N}$, assuming that the projected radius of the *SWAS* beam at the distance of the source ($r_{SWAS} = 0.094$ pc) is a lower limit to the line-of-sight extent of the cloud. The virial mass of a clump with $n = 10^{5.5}$ cm^{-3} is $M_{vir} = 5\ \sigma^2 r_{cl}/G \approx 400\ M_\odot$ (Bertoldi & McKee 1992), where $\sigma = \Delta v/2.355 \approx 1$ km $^{-1}$ is the one-dimensional gas velocity dispersion and G is the gravitational constant. Thus, M_{vir} is more than 3 orders of magnitude larger than the clump mass. Clearly, self-gravity is unimportant in this case, and it is hard to see how the resulting high density contrast could be maintained. We therefore consider it unlikely that high densities of $n \gtrsim 10^5$ cm^{-3} dominate throughout the cloud as suggested by the PDR model without preshielding.

We also consider it unlikely that the bulk of the gas in MCLD 123.5+24.9 is at the cloud-average density of $n \sim 500$ cm^{-3}, as this is in clear conflict with the observed line intensities. For densities this low, most of the carbon should be in ionized or neutral form, and the [C I] line flux densities should be orders of magnitude larger than for the CO rotational transitions.

The same conclusion would not only apply to MCLD 123.5+24.9 but to other observations published in the literature. The flux density ratios are within the range of ratios that can be derived from published observations of translucent clouds, although some of the ratios for MCLD 123.5+24.9 are at the lower end of this range (Table 3). Moreover, similar line ratios are found for translucent clouds observed with *SWAS* toward the Galactic mid-plane

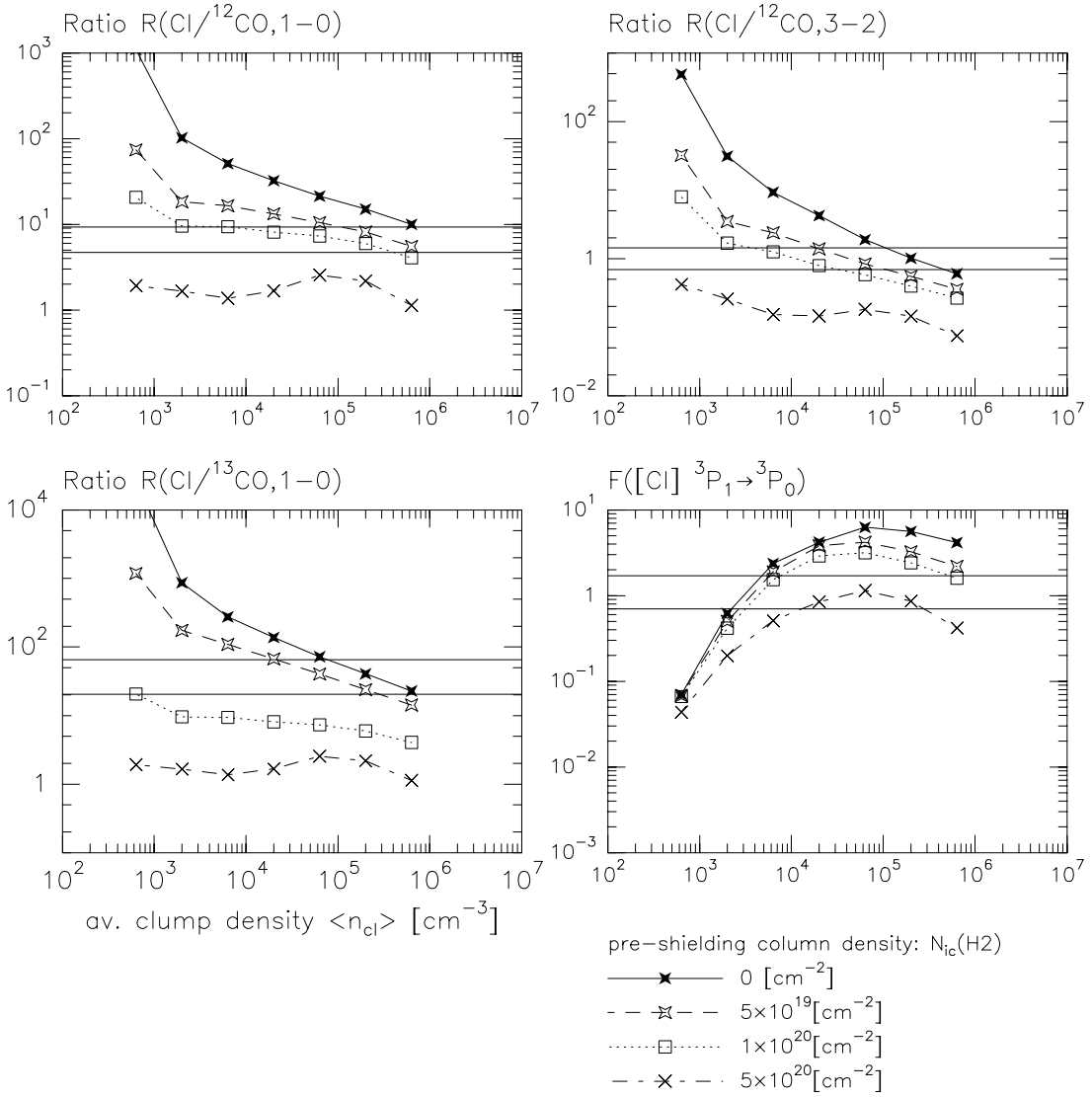


FIG. 7.—PDR model results for clumps in the ISRF and preshielding by a molecular hydrogen column density of $N_{ic}(H_2)$ in a surrounding halo or interclump medium. *Upper panels*: [C I] $^3P_1 \rightarrow {}^3P_0$ to ^{12}CO $J = 1 \rightarrow 0$ ratio (*left*) and [C I] to ^{12}CO $J = 3 \rightarrow 2$ ratio (*right*) as a function of the average clump density for different preshielding column densities $N_{ic}(H_2)$. *Lower panels*: Same plot for the [C I] to ^{13}CO $J = 1 \rightarrow 0$ ratio (*left*) and the [C I] $^3P_1 \rightarrow {}^3P_0$ line flux density (*right*). *Horizontal lines*: Range observed toward MCLD 123.5+24.9.

(F. Bensch et al. 2003, in preparation) and for the global emission observed toward a number of galaxies (Gerin & Phillips 2000).

5.2. *Clumps in an Interclump Medium?*

It is not unreasonable to assume the presence of a interclump medium, as a continuous transition of the dense gas in the clump to the ambient diffuse and neutral medium is expected. Evidence for an ambient gas with lower density for MCLD 123.5+24.9 is provided with the H I observations by (Meyerdierks, Heithausen, & Reif 1991). Moreover, only a small H_2 column density of $N_{ic}(H_2) = (0.5\text{–}1) \times 10^{20}$ cm^{-2} in the interclump medium is sufficient to significantly reduce the [C I]/CO line ratios of the embedded clumps. This is not a substantial fraction of the total visual extinction observed toward MCLD 123.5+24.9. The comparison of the observed [C I] to CO line ratios with PDR models of clumps with a preshielding gas suggests moderate densities of $\sim 10^4$ cm^{-3} for the embedded clumps, which is consistent with the density suggested by the spatially extended ^{12}CO $J = 3 \rightarrow 2$ emission. Thus, it is plausible that the low [C I] flux densities and [C I] to CO line ratios result from denser (CO) gas that is shielded by molecular hydrogen in surrounding gas of lower density.

The PDR models only constrain the H_2 column density of the preshielding material, and the density of the gas cannot be ascertained using these models. However, an upper limit can be inferred from the constraint that the [C I] $^3P_1 \rightarrow {}^3P_0$ emission from the interclump material is negligible, which suggests a density smaller than the critical density of the [C I] transition, 10^3 cm^{-3}. This preshielding gas can be an interclump medium or a surface layer (halo) enclosing the denser clumps.

5.3. *The Chemical Network of the PDR Model*

Additional uncertainties in the PDR model are related to the chemical network and, in particular, to the uncertainties in the sulphur chemistry and the degree of sulphur depletion

in the gas phase. Heithausen et al. (2001) present PDR models for the [C I] and CO observations of two intermediate-velocity clouds (IVC 135+54−46 and the Draco Nebula), employing the same code we use for our simulations. While the [C I]/CO ratios for IVC 135+54−46 and MCLD 123.5+24.9 agree within the measurement accuracy, the line ratios noted for the Draco Nebula are somewhat larger [$R(\mathrm{C\ I}/^{12}\mathrm{CO},\ 2\text{–}1) = 4.9 \pm 1.8$ CO and $R(\mathrm{C\ I}/^{12}\mathrm{CO},\ 3\text{–}2) = 1.9 \pm 0.6$, compared to 1.37 ± 0.41 and 1.06 ± 0.37 for MCLD 123.5+24.9]. They quote a density of 5×10^4 cm^{-3}, a factor of 10 smaller than for our PDR model without preshielding. In addition to the larger line ratios for the Draco Nebula, the difference can be largely attributed to their reduced chemical network in their PDR model, excluding sulfur-bearing species. If present with a significant abundance, sulfur has a profound influence on the carbon abundance (Sternberg & Dalgarno 1995; Flower et al. 1994; Tielens & Hollenbach 1985). Observations of SO reveal high abundances for MCLD 123.5+24.9 and suggest that sulfur is undepleted. We therefore include sulfur with an abundance of $X_{S^+} = 2.8 \times 10^{-5}$ in our models, resulting in an increased [C I] line flux density for clumps with $n \gtrsim 10^{4.5}$ cm^{-3} and $\chi \lesssim 1$. Typically, the [C I] $^3P_1 \rightarrow {}^3P_0$ line is brighter by a factor of 2–6 for models with sulfur. This is partly compensated by the additional hydrogen-carbon species, which somewhat reduce the abundance of neutral carbon. Overall, the [C I] to CO line flux density ratios in our models are larger by up to a factor of 2.5 compared to the network presented by Störzer, Stutzki, & Sternberg (1996). Thus, the uncertainties in the sulfur abundance can change the clump densities deduced from the PDR model by a factor of a few but not by an order of magnitude or more. We therefore conclude that the low [C I] intensities and [C I] to CO ratios do not necessarily reflect a low sulfur abundance.

6. CONCLUSIONS AND SUMMARY

Using the *Submillimeter Wave Astronomy Satellite* (*SWAS*), we made the first [C I] $^3P_1 \rightarrow {}^3P_0$ map of a translucent molecular cloud. MCLD 123.5+24.9 is one of the best studied high-latitude translucent clouds with a large observational data base providing constraints on cloud parameters such as the visual extinction, chemical composition, and the strength of the FUV field. This makes MCLD 123.5+24.9 an ideal test case for a PDR model. The comparison of the [C I] data with observations of low-J ^{12}CO and ^{13}CO transition from ground-based telescopes can be summarized as follows:

1. The [C I] is spatially extended and generally follows the region with bright ^{12}CO emission. The [C I] to low-J ^{12}CO line integrated intensity ratio shows little to no variation across the cloud and is at the low end of the range typically found for translucent clouds in the literature.

2. The [C I] to ^{13}CO line ratios show a significant variation, with the ^{13}CO line profiles having smaller widths than the [C I] and ^{12}CO profiles.

3. The total line flux density of the [C I] $^3P_1 \rightarrow {}^3P_0$ transition is ~50% of the flux emitted by three lowest ^{12}CO rotational transitions. Cooling by CO and/or the fine-structure transition of ionized carbon is therefore likely to dominate over the cooling by [C I].

4. Assuming LTE excitation conditions with $T_{ex} = 8$ K, we derive neutral carbon column densities between 0.25 and 1.0×10^{17} cm^{-2} and a C to CO column density ratio between 0.2 and 1.1.

The C to CO column density ratio has to be considered as an upper limit. With the interstellar radiation field as an external heating source, the temperature is expected to decrease from the cloud surface where neutral carbon is abundant toward the interior. We therefore conclude that the assumption of a constant excitation temperature with the LTE approximation underestimates the CO column density derived from the ^{13}CO line-integrated intensity and overestimates the neutral carbon column density.

Comparison with PDR model predictions shows that the relatively low [C I]/CO intensity ratio observed throughout MCLD 123.5+24.9 and for other translucent clouds would require high densities in excess of 10^5 cm^{-3}, unless we assume the presence of preshielding gas with a low density ($n < 10^3$ cm^{-3}). This gas might enclose the denser clumps as a surface layer or form a more extended interclump medium. It does not contribute significantly to the observed line emission, but the FUV line absorption of the molecular hydrogen in the interclump medium significantly reduces the photodissociation of CO for the embedded clumps. As a consequence, the [C I] line flux density and the [C I] to CO line ratio are reduced. An interclump medium with a relatively small H_2 column density of the order of $N_{ic}(H_2) \approx (0.5\text{–}1) \times 10^{20}$ is sufficient to model the observed [C I] flux density and [C I] to CO line ratios with embedded clumps of density ~10^4 cm^{-3}, a density consistent with the observation that the ^{12}CO $J = 3 \rightarrow 2$ transition is nearly (but not fully) thermalized.

We acknowledge the support provided by the DLR through grants 50 0090 090 and 50 0099 011. F. B. is supported by the Deutsche Forschungsgemeinschaft DFG (research stipend Be 2412/1-1). The KOSMA 3 m radio telescope at Gornergrat-Süd Observatory is jointly operated by the University of Cologne and Bonn as well as special funding from the Land Nordrhein-Westfalen. The receiver development was partly funded by the Bundesminister für Forschung and Technologie. The observatory is administered by the Internationale Stiftung Hochalpine Forschungsstationen Jungfraujoch und Gornergrat, Bern. This research has made use of NASA's Astrophysics Data System Abstract Service.

REFERENCES

Bensch, F., Stutzki, J., & Ossenkopf, V. 2001, A&A, 366, 636
Bernard, J. P., et al. 1999, A&A, 347, 640
Bertoldi, F., & McKee, C. F. 1992, ApJ, 395, 140
Castets, A., Duvert, G., Dutrey, A., Bally, J., Langer, W. D., & Wilson, R. W. 1990, A&A, 234, 469
Chièze, J.-P., Pineau des Forêts, G., & Herbst, E. 1991, ApJ, 373, 110
Draine, B. T. 1978, ApJS, 36, 595
Falgarone, E., Panis, J.-F., Heithausen, A., Pérault, M., Stutzki, J., Puget, J.-L., & Bensch, F. 1998, A&A, 331, 669
Flower, D. R., Le Bourlot, J., Pineau des Forêts, G., & Roueff, E. 1994, A&A, 282, 225
Gerin, M., Falgarone, E., Joulain, K., Kopp, M., Le Bourlot, J., Pineau des Forêts, G., Roueff, E., & Schilke, P. 1997, A&A, 318, 579
Gerin, M., & Phillips, T. G. 2000, ApJ, 537, 644
Gierens, K. M., Stutzki, J., & Winnewisser, G. 1992, A&A, 259, 271
Grossmann, V., & Heithausen, A. 1992, A&A, 264, 195
Grossmann, V., Heithausen, A., Meyerdierks, H., & Mebold, U. 1990, A&A, 240, 400

Heithausen, A., Bertoldi, F., & Bensch, F. 2002, A&A, 383, 591
Heithausen, A., Corneliussen, U., & Grossmann, V. 1995, A&A, 301, 941
Heithausen, A., & Thaddeus, P. 1990, ApJ, 353, L49
Heithausen, A., Weiss, A., Kerp, J., & Fritz, T. 2001, ApJ, 561, 238
Hollenbach, D. J., Takahashi, T., & Tielens, A. G. G. M. 1991, ApJ, 377, 192
Hollenbach, D. J., & Tielens, A. G. G. M. 1999, Rev. Mod. Phys., 71, 173
Ingalls, J. G., Bania, T. M., & Jackson J. M. 1994, ApJ, 431, L139
Ingalls, J. G., Chamberlin, R. A., Bania, T. M., Jackson, J. M., Lane, A. P., & Stark, A. A. 1997, ApJ, 479, 296
Kaufman, M. J., Wolfire, M. G., Hollenbach, D. J., & Luhman, M. L. 1999, ApJ, 527, 795
Keene, J., Blake, G. A., & Phillips, T. G. 1987, ApJ, 313, 396
Köster, B. 1998, Ph.D. thesis, Univ. Cologne
Kramer, C., Stutzki, J., & Winnewisser, G. 1996, A&A, 307, 915
Le Bourlot, J., Pineau des Forêts, G., Roueff, E., & Schilke, P. 1993, ApJ, 416, L84
Maezawa, H., et al. 1999, ApJ, 524, L129
Matsuhara, H., et al. 1997, ApJ, 490, 744
Melnick, G. J., et al. 2000, ApJ, 539, L77
Meyerdierks, H., Heithausen, A., & Reif, K. 1991, A&A, 245, 247
Plume, R., Jaffe, D. T., & Keene, J. 1994, ApJ, 425, L49
Plume, R., et al. 2000, ApJ, 539, L133
Rohlfs, K., & Wilson, T. L. 2000, Tools of Radio Astronomy (3d ed.; Berlin: Springer)
Savage, B. D., & Sembach, K. R. 1996, ARA&A, 34, 279
Schreiber, W., Wouterloot, J. G. A., Heithausen, A., & Winnewisser, G. 1993, A&A, 276, L5
Smith, D., & Adams, N. G. 1980, ApJ, 242, 424
Stark, R., & van Dishoeck, E. F. 1994, A&A, 286, L43
Stark, R., Wesselius, P. R., van Dishoeck, E. F., & Laureijs, R. J. 1996, A&A, 311, 282
Sternberg, A., & Dalgarno, A. 1995, ApJS, 99, 565
Störzer, H., Stutzki, J., & Sternberg, A. 1996, A&A, 310, 592
———. 1997, A&A, 323, L13
Tatematsu, K., Jaffe, D. T., Plume, R., Evans II, N. J., & Keene, J. 1999, ApJ, 526, 295
Tielens, A. G. G. M., & Hollenbach, D. 1985, ApJ, 291, 722
Timmermann, R., Köster, B., & Stutzki, J. 1998, A&A, 336, L53
van Dishoeck, E. F., & Black, J. H. 1986, ApJS, 62, 109
———. 1988, ApJ, 334, 771
Watson, W. D., Anicich, V. G., & Huntress, Jr., W. T. 1976, ApJ, 205, L165
Zagury, F., Boulanger, F., & Banchet, V. 1999, A&A, 352, 645